Nanoscale

PAPER

View Article Online
View Journal | View Issue

Check for updates

Cite this: *Nanoscale*, 2024, **16**, 9123

High-efficiency electrodeposition of magnesium alloy-based anodes for ultra-stable rechargeable magnesium-ion batteries†

Xiao Chai, ‡ Yan Xin,‡ Bijiao He, Fang Zhang, Haokai Xie and Huajun Tian *

Rechargeable magnesium batteries (RMBs) have attracted much attention because of their high theoretical volumetric capacity and high safety. However, the uneven deposition behavior, harmful corrosion reaction and poor stability of magnesium metal anodes have hindered the practical application of RMBs. Herein, we propose a facile alloy electrodeposition method to construct an artificial layer on an Mg anode. Experimental results show that the polarization of the symmetric magnesium alloy-based (Mg–Sn@Mg and Mg–Bi@Mg) cells is significantly reduced (~0.05 V) at a current density of 0.1 mA cm^{-2}. The symmetric cells using the prepared Mg alloy anodes exhibited lower voltage hysteresis and ultra-stable cycling performance at a higher density of 1.0 mA cm^{-2} over 700 h. The *in situ* optical microscopy study clearly demonstrated that the Mg dendrite formation was successfully retarded by the designed Mg–Sn and Mg–Bi alloy artificial protective layer on Mg anodes. The superiority of Mg–Sn@Mg and Mg–Bi@Mg was further confirmed in full cells using Mo_6S_8 as the cathode. Compared with the Mo_6S_8//Mg full cell, the Mo_6S_8//Mg–Sn@Mg and Mo_6S_8//Mg–Bi@Mg full cells maintained an ultra-stable electrochemical performance even after 5000 cycles. This proof-of-concept provides a novel scope for the artificial coating layers on Mg anodes prepared by alloy electrodeposition and can be extended to other alloy anodes (*i.e.* Mg–Cu@Mg and so on). This work provides an avenue for the design of practical and high-performance RMBs and beyond.

Received 28th February 2024,
Accepted 4th April 2024

DOI: 10.1039/d4nr00842a

rsc.li/nanoscale

Published on 04 travnja 2024. Downloaded on 5.6.2026. 21:53:00.

Introduction

Growing concerns about global environmental and energy sustainability are now driving research and development of clean energy storage technologies.[1–4] The dominant Li-ion batteries (LIBs) in the energy storage landscape are facing constraints in meeting the development of vehicle electrification and large-scale energy storage due to their limited energy density and scarce lithium resources.[5–9] Rechargeable magnesium-ion batteries (RMBs) have attracted increasing attention due to their high capacity, natural abundance, low cost and environmental friendliness to meet the rapid demand for renewable energy storage systems.[10–13]

Magnesium metal has a low redox potential (−2.37 V *vs.* SHE), a high volumetric capacity (3733 mA h cm^{-3}), good chemical stability and high terrestrial abundance.[9,14–16] Aurbach *et al.* created the initial magnesium battery prototype in 2000.[17] Although there has been significant advancement in research on cathodes and electrolytes since then, one of the main obstacles to magnesium ion battery development remains to be the incompatibility of anodes, electrolytes, and cathodes.[18–20] However, unlike other metal anodes (such as lithium), the usage of magnesium metal anodes presents a far greater challenge due to the creation of a passivation layer on magnesium metal in the majority of organic electrolytes.[21–23] This Mg^{2+} passivation layer, which consists mainly of magnesium oxide (MgO) or magnesium hydroxide ($Mg(OH)_2$), is thought to form naturally on the magnesium surface and can lead to irreversible magnesium plating/stripping.[12,24,25] Therefore, a great deal of research has focused on the invention of new electrolytes to reduce the formation of insulating layers in the early stages of research.[24,26–28] Facing passivation problems in conventional $Mg(TFSI)_2$-based electrolytes and the issue of "magnesium dendrites" in Grignard's agents or an all-phenyl compound (APC) under extreme conditions (high current density or large areal capacity), it is crucial to develop magnesium-metal anodes that are not passivated and free of dendrites in conventional electrolytes.[8,29–31]

The current optimization strategies for Mg anodes mainly include electrolyte modification,[32–34] constructing the metal–

Key Laboratory of Power Station Energy Transfer Conversion and System of Ministry of Education and School of Energy Power and Mechanical Engineering, and Beijing Laboratory of New Energy Storage Technology, North China Electric Power University, Beijing, 102206, China. E-mail: Huajun.Tian@ncepu.edu.cn

†Electronic supplementary information (ESI) available. See DOI: https://doi.org/10.1039/d4nr00842a

‡These authors contributed equally to this work.

Published on 04 travnja 2024. Downloaded on 5.6.2026. 21:53:00.

organic skeleton,[35,36] and designing an artificial solid electrolyte interphase (SEI).[37–39] In particular, in recent years, some researchers have modified magnesium anodes by designing artificial SEIs, which can enhance the stability of the anode interface. Li *et al.*[40] added I_2 to the electrolyte to form a MgI_2-based protective layer on the magnesium anode. Zhang *et al.*[41] developed a Ge-based alloy layer on the Mg metal anode by adding an excessive amount of $GeCl_4$. Li *et al.*[42] designed a protective layer on a Mg metal anode by applying $SiCl_4$/DME solution, and a protective layer enriched with $MgCl_2$ at the top and Si at the bottom was designed. Wang *et al.*[43] electrochemically pretreated magnesium and a DOL-based SEI was formed on the Mg metal surface. These efforts can effectively inhibit the surface passivation between Mg and the electrolyte and improve the kinetics of Mg plating/stripping, thus improving cycling stability and multiplicative performance.[44,45] However, the majority of magnesium anode modification methods usually require complex preparation processes and pretreatment procedures and are expensive to prepare.[46,47] Electrodeposition is a centuries-old technique for the synthesis of inorganic materials, conductive polymers and metal–organics.[48–52] It is a simple, low-cost, efficient and easy-to-control method for the preparation of surface layers.[52,53] Simultaneously, electrodeposition is a simple, low-cost, efficient and easy-to-control technique for producing thin metal films on conductive substrates.[54]

In this work, a facile and high-efficiency electrodeposition was used to deposit Mg–Sn@Mg and Mg–Bi@Mg artificial protective layers on Mg metal surfaces, which can be stably cycled for a long time in an APC electrolyte. The Mg–Sn@Mg and Mg–Bi@Mg layers offer a rapid channel for the transport of Mg^{2+}, and they can also significantly enhance the inhomogeneous Mg plating/stripping behavior, hence facilitating the uniform deposition of Mg^{2+} and enhancing the performance of RMBs. Hence, Mg–Sn@Mg and Mg–Bi@Mg demonstrate a remarkable long life of over 1000 h with a low polarization voltage (0.2 mA cm^{-2}; 0.2 mA h cm^{-2}) and excellent multiplicative performance (at different current densities from 0.1 to 1 mA cm^{-2}) in symmetric cell tests. Even at high current densities (1.0 mA cm^{-2}; 1.0 mA h cm^{-2}), the Mg–Bi@Mg and Mg–Sn@Mg symmetric cells exhibit enhanced cyclability and lower polarization voltages than the bare Mg symmetric cell. In addition, when coupled with Mo_6S_8 cathodes, the full cells exhibit extraordinary electrochemical performance even after 5000 cycles at 10 C.

Results and discussion

The Mg–Sn@Mg and Mg–Bi@Mg anodes were prepared using alloy electrodeposition (detailed information is provided in the Experimental section). As shown in the Scanning Electron Microscopy (SEM) images of Fig. 1a and b, homogeneous coatings of Mg–Sn@Mg and Mg–Bi@Mg with a 3D structure were formed on Mg surfaces after alloy electrodeposition. The EDS elemental mapping images (Fig. 1c) show the uniform distribution of the two elements (Mg, Sn and Mg, Bi) on the surface of magnesium metal, respectively. The cross-sectional SEM images (Fig. S1 and S2†) show that the Mg alloy layers are densely and uniformly adhered to the Mg substrate. The thicknesses of Mg–Sn and Mg–Bi are 3.5 μm and 2.2 μm, respectively. The compositions of Mg–Sn@Mg and Mg–Bi@Mg were identified by X-ray diffraction (XRD) measurements. Fig. 1d and g confirm that Mg, Sn, and Mg, Bi metals are observed in the corresponding protective layers, respectively (Mg (JCPDS no. 35-0821), Bi (JCPDS no. 44-1246) and Sn (JCPDS no. 65-0296)). The above observations suggest that Mg–Sn@Mg and Mg–Bi@Mg anodes were successfully prepared by this simple alloy electrodeposition. We also used alloy electrodeposition to prepare different protective layers on Mg foil, such as Mg–Cu@Mg. XRD pattern demonstrates the Mg–Cu@Mg coating as shown in Fig. S3.† The SEM image in Fig. S4† shows that the Mg–Cu protective layer is uniformly distributed on the magnesium substrate.

X-ray photoelectron spectroscopy (XPS) was used to characterize Mg–Sn@Mg and Mg–Bi@Mg anodes. The full XPS spectrum of Mg–Sn@Mg in Fig. S5† indicates the presence of the elements Mg and Sn in the as-prepared sample after alloy electrodeposition. The high-resolution XPS spectrum of the Mg 1s region (Fig. 1e and h) can be fitted to a Gaussian peak centered at 1303.5 eV, indicating the presence of Mg. The XPS spectrum of the Sn 3d region (Fig. 1f) can be resolved into two peaks, Sn $3d_{5/2}$ and Sn $3d_{3/2}$, with high resolution corresponding to binding energies of 486.5 eV and 495 eV, respectively. Similarly, the full XPS spectrum of Mg–Bi@Mg in Fig. S6† shows the presence of Mg and Bi elements in the sample after alloy electrodeposition. The high-resolution XPS spectrum of the Bi 4f region (Fig. 1i) can be resolved into four peaks corresponding to four Gaussian peaks centered at 156.0 eV, 158.5 eV, 161.2 eV, and 163.8 eV, respectively. Corresponding to the XPS results of bare Mg in Fig. S7,† it reconfirms the successful preparation of Mg–Sn@Mg and Mg–Bi@Mg anodes.

The all-phenyl complex (APC) electrolyte was used in RMBs. The plating/stripping process of the APC electrolyte was tested using a three-electrode cell (Fig. S8†). The reversibility of the magnesium plating/stripping reaction was tested using a symmetric cell configuration consisting of two identical magnesium electrodes in an APC electrolyte. Fig. 2a shows the voltage profiles of the Mg–Sn@Mg//Mg–Sn@Mg, Mg–Bi@Mg//Mg–Bi@Mg and bare Mg//bare Mg symmetric cells at a current density of 0.1 mA cm^{-2} (0.1 mA h cm^{-2}). The bare Mg electrode showed an extremely high initial polarization of 0.36 V (Fig. 2b). The polarization gradually decreased during further cycles, reaching ~0.10 V at the 25th cycle. In contrast, both Mg–Sn@Mg and Mg–Bi@Mg electrodes achieved high operational stability of more than 1000 h with slight voltage fluctuations, and stabilized at ~0.05 V. This indicates that due to the presence of the alloy protective layer, the electrochemical activity and reversibility of the Mg metal anode are improved. In addition, Mg–Cu@Mg symmetric cells were assembled to verify that the Mg plating/stripping was reversible. As shown in

 This journal is © The Royal Society of Chemistry 2024

Published on 04 travnja 2024. Downloaded on 5.6.2026. 21:53:00.

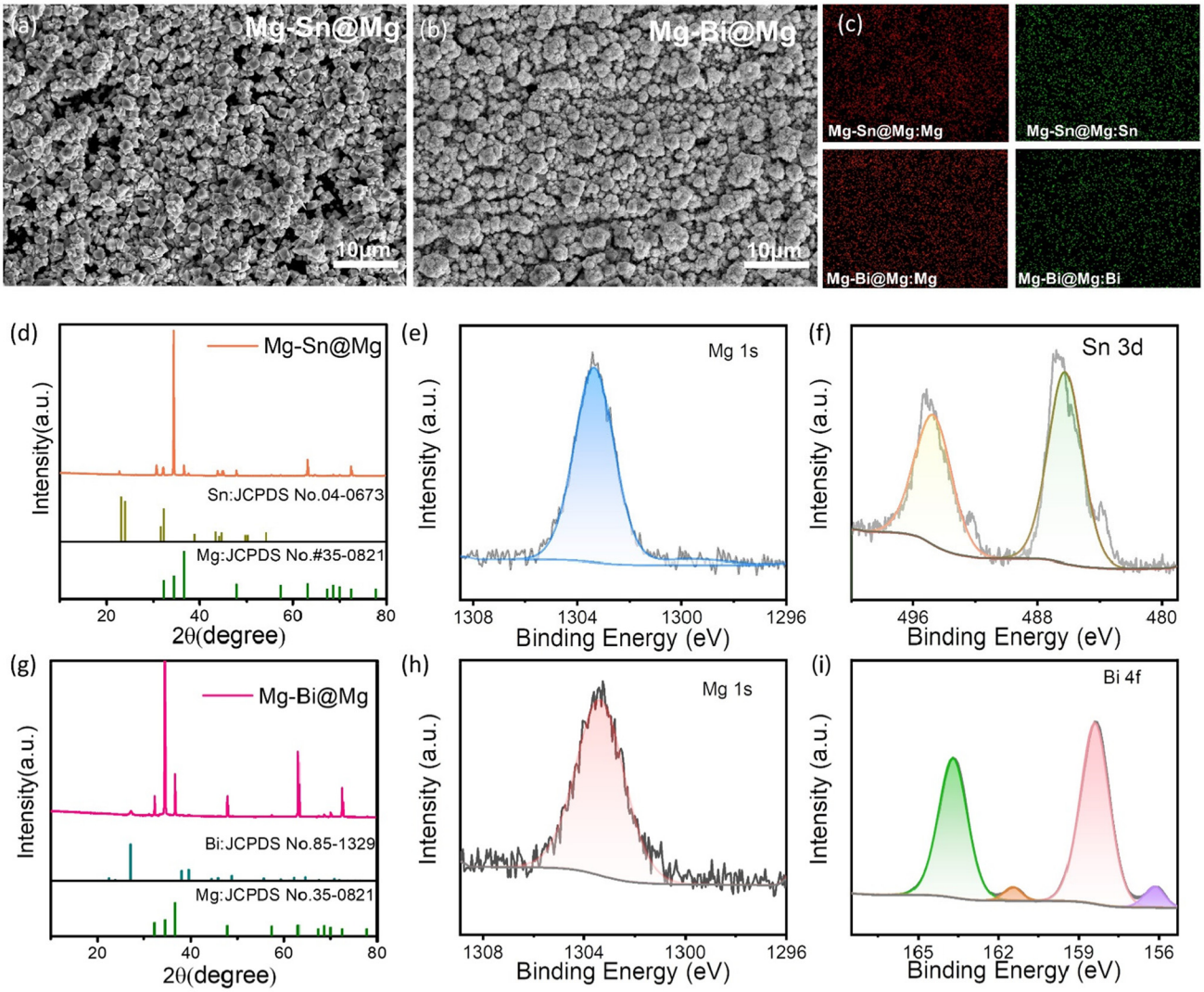

Fig. 1 SEM images of (a) Mg–Sn@Mg and (b) Mg–Bi@Mg. (c) EDS elemental mapping images of Mg–Sn@Mg and Mg–Bi@Mg. (d) XRD patterns of Mg–Sn@Mg. XPS analysis of the survey spectrum: (e) Mg 1s and (f) Sn 3d. (g) XRD patterns of Mg–Bi @Mg. XPS analysis of the survey spectrum: (h) Mg 1s and (i) Bi 4f.

Fig. S9,† at a current density of 0.1 mA cm^{-2}, Mg–Cu@Mg// Mg–Cu@Mg achieves a stable cycle of more than 700 h and a low polarization of 0.065 V.

Fig. 2c–f show the reversibility of Mg plating/stripping behaviors at different current densities, respectively. When the areal capacity was increased to 0.2 mA h cm^{-2} (Fig. 2c), the voltage hysteresis of the bare magnesium cell showed serious fluctuations during cycling, and the voltage suddenly plummeted after 619 h. A sharp drop in voltage in a symmetrical cell is usually considered a sign of a short circuit.[55–57] Similarly, the polarization of the Mg–Sn@Mg and Mg–Bi@Mg symmetric cells gradually decreased and was lower than that of bare Mg cells. The Mg–Sn@Mg and Mg–Bi@Mg anodes had a low voltage hysteresis of ≈0.07 V (Fig. 2d) and negligible voltage fluctuations for more than 1000 h. The superiority of Mg–Sn@Mg and Mg–Bi@Mg in particular was again demonstrated at a high current density of 1 mA cm^{-2} and a higher areal capacity of 1 mA h cm^{-2}. As shown in Fig. 2e and f, the bare Mg symmetric cell suffers from severe voltage fluctuations and only lasts for 125 h before short-circuiting. Impressively, the Mg–Sn@Mg and Mg–Bi@Mg cells were able to achieve stability at low average overpotentials of 0.18 V and 0.14 V, respectively, for more than 700 h. The electrochemical performance of the above symmetric cells demonstrates that bare Mg has higher voltage hysteresis and shorter lifetime compared to Mg–Sn@Mg and Mg–Bi@Mg. It is verified that the electrochemical activity and reversibility of magnesium-based alloy anodes (Mg–Sn@Mg and Mg–Bi@Mg) are substantially improved compared with those of bare Mg metal anodes.

Galvanostatic tests on symmetric cells evaluated the superiority of Mg–Sn@Mg and Mg–Bi@Mg in terms of cycling stability. The rate capability of the symmetric cells (bare Mg//bare

Published on 04 travnja 2024. Downloaded on 5.6.2026. 21:53:00.

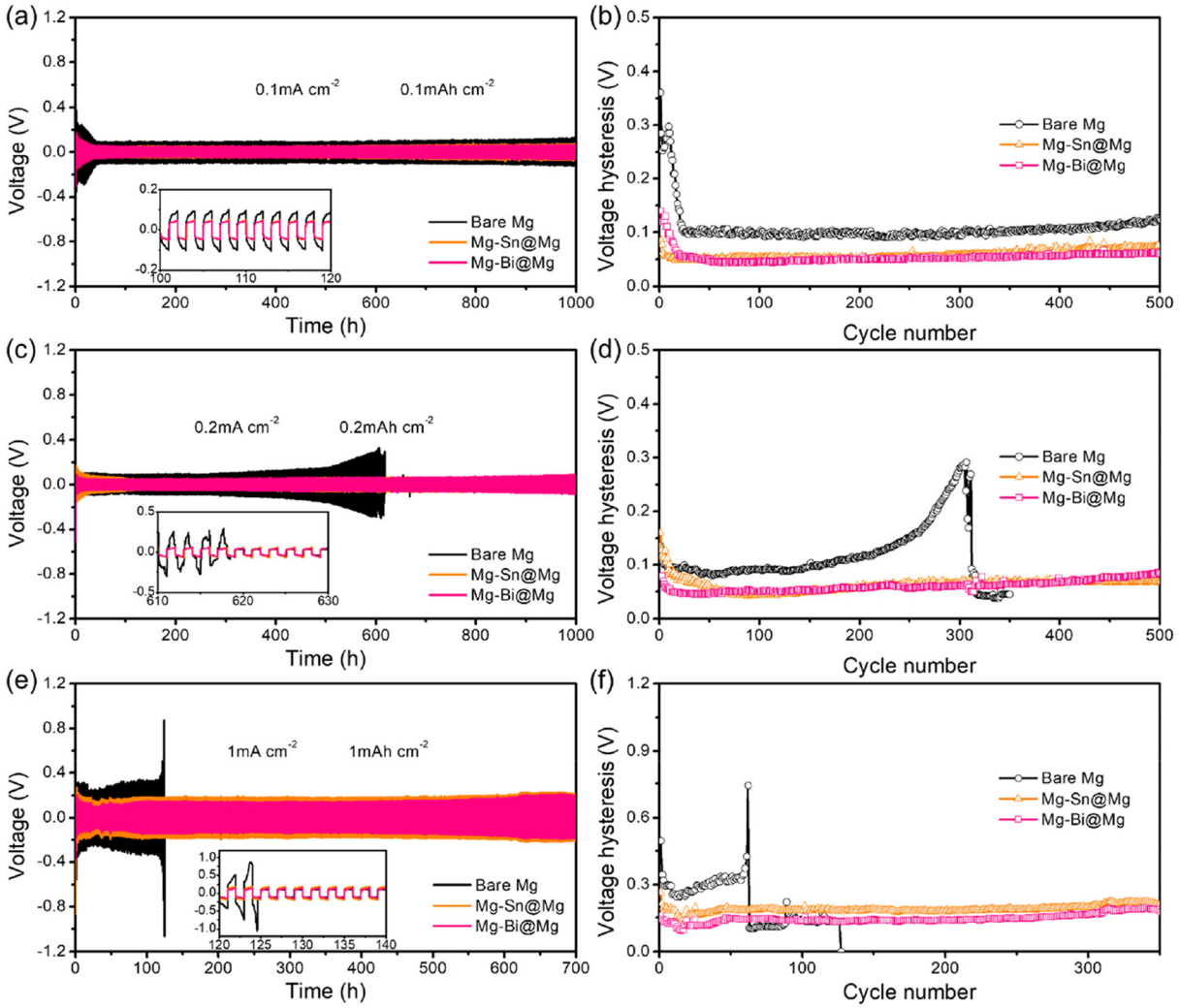

Fig. 2 (a) Cycling performance and (b) the corresponding voltage hysteresis of symmetric cells with bare Mg, Mg–Sn@Mg and Mg–Bi@Mg electrodes at 0.1 mA cm^{-2} (areal capacity: 0.1 mA h cm^{-2}). (c) Cycling performance and (d) the corresponding voltage hysteresis of symmetric cells with bare Mg, Mg–Sn@Mg and Mg–Bi@Mg electrodes at 0.2 mA cm^{-2} (0.2 mA h cm^{-2}). (e) Cycling performance and (f) the corresponding voltage hysteresis of symmetric cells with bare Mg, Mg–Sn@Mg and Mg–Bi@Mg electrodes at 1 mA cm^{-2} (areal capacity: 1.0 mA h cm^{-2}).

Mg, Mg–Sn@Mg//Mg–Sn@Mg, Mg–Bi@Mg//Mg–Bi@Mg) was verified at different current densities from 0.1 to 1.0 mA cm^{-2}. The polarization voltages of the cells with Mg–Sn@Mg and Mg–Bi@Mg are consistently lower than that of the cells with bare Mg at all current densities (Fig. 3a). More importantly, the higher the applied current density, the greater the difference in polarization voltages between the three cells. Furthermore, the magnesium deposition kinetics can be quantified by the exchange current density (i_0), which is calculated according to the following equation:[58]

$$i = i_0 \frac{F}{RT} \cdot \frac{\eta}{2} \quad (1)$$

where i is the operating current density, F is Faraday's constant, η is the total overpotential, R is the gas constant, and T is the absolute temperature.

The total overpotential was obtained from the electrostatic tests of symmetrical cells at different current densities (Fig. 3a). As shown in Fig. 3b, the i_0 of Mg–Sn@Mg and Mg–Bi@Mg is 0.211 and 0.243 mA cm^{-2}, respectively, which is much higher than that of bare Mg (0.136 mA cm^{-2}). The kinetics of Mg deposition enhanced by Mg–Sn@Mg and Mg–Bi@Mg shows that Mg–Sn@Mg and Mg–Bi@Mg can effectively improve the Mg deposition/dissolution behavior. To study the electrochemical dynamics and performance of Mg–Sn@Mg and Mg–Bi@Mg with stable Mg deposition/dissolution behavior, various electrochemical analyses were carried out on symmetric cells. Cyclic voltammetry (CV) measurements of the symmetric cells were performed at a scan rate of 1 mV s^{-1}. Fig. 3c shows that the combined peak areas of Mg–Sn@Mg and Mg–Bi@Mg symmetric cells are larger than that of bare Mg cell, which indicates the improved electrochemical redox activity of Mg deposition. From the contact angle tests, the

 This journal is © The Royal Society of Chemistry 2024

Published on 04 travnja 2024. Downloaded on 5.6.2026. 21:53:00.

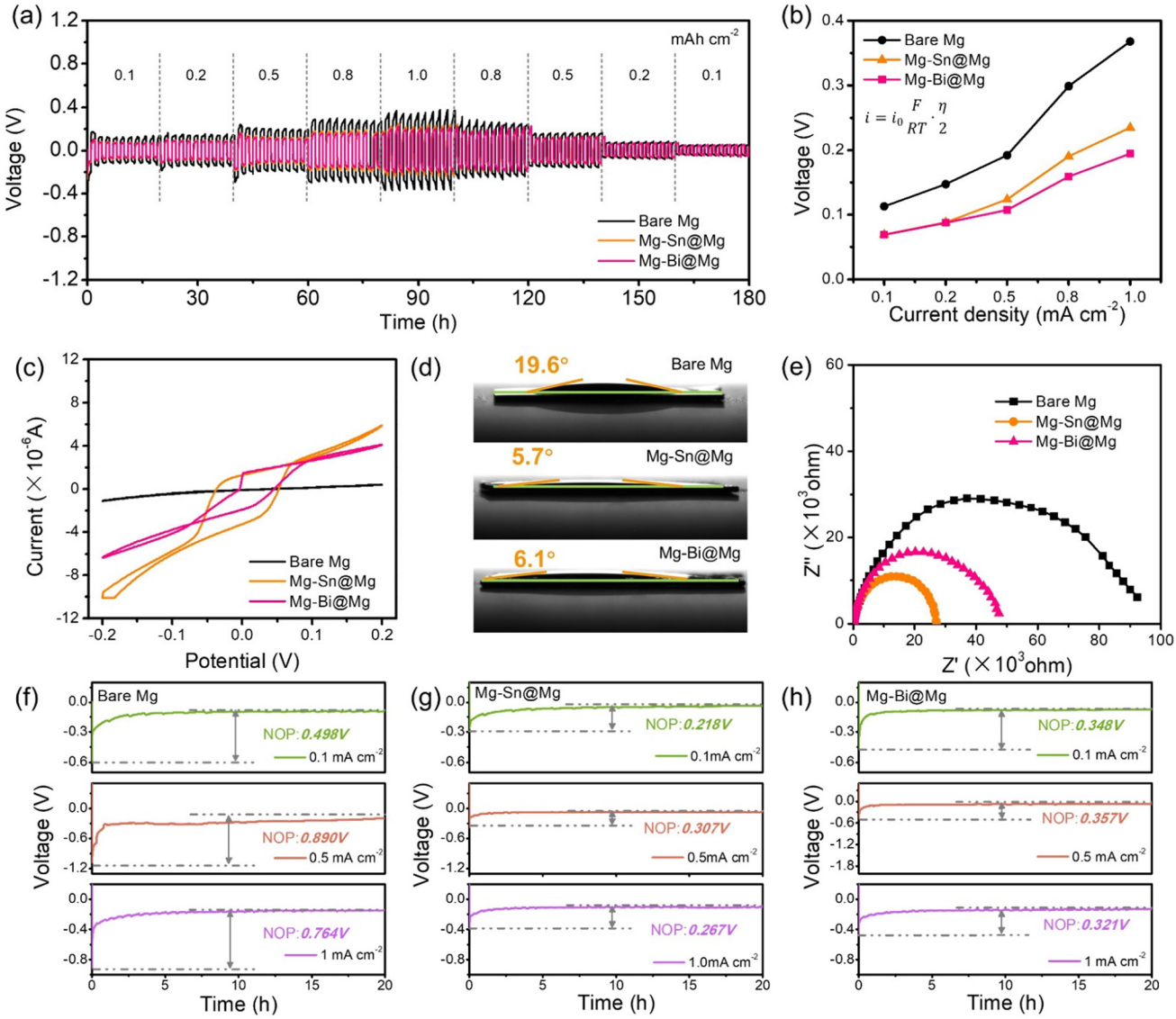

Fig. 3 (a) Rate capability of symmetric cells at different current densities from 0.1 to 2.0 mA cm^{-2} and (b) corresponding exchange current densities of bare Mg, Mg–Sn@Mg and Mg–Bi@Mg. (c) CV curves of symmetric cells (bare Mg//bare Mg, Mg–Sn@Mg//Mg–Sn@Mg and Mg–Bi@Mg//Mg–Bi@Mg) obtained at a scan rate of 1 mV s^{-1}. (d) Contact angles of the APC electrolyte on bare Mg, Mg–Sn@Mg and Mg–Bi@Mg, respectively. (e) EIS for the Mg–Mg symmetric cells using bare Mg, Mg–Sn@Mg and Mg–Bi@Mg. (f–h) Voltage profiles of Mg deposition on (f) bare Mg, (g) Mg–Sn@Mg and (h) Mg–Bi@Mg at different current densities from 0.1 to 1 mA cm^{-2}.

interfacial performance of the Mg anode was examined by whether the anode surface sufficiently absorbed the APC electrolyte. As shown in Fig. 3d, the affinity performance of Mg–Sn@Mg (5.7°) and Mg–Bi@Mg (6.1°) was enhanced compared to that of bare Mg (19.6°). Similarly, the affinity property of Mg–Cu@Mg (4.1°) is also enhanced as shown in Fig. S10.† This suggests that the alloy-based protective layer prepared by alloy electrodeposition may provide abundant active sites and enhance the transport/diffusion of Mg^{2+} ions. To further confirm the above findings, electrochemical impedance spectroscopy (EIS) analysis of the symmetric cells was performed to verify the enhanced electrochemical stability and deposition kinetics of Mg–Sn@Mg and Mg–Bi@Mg (Fig. 3e and Table S1†). Compared to the charge transfer resistance (R_{ct}) of the bare Mg symmetric cell (85 067 Ω), the R_{ct} of the symmetric cells of Mg–Sn@Mg (26 000 Ω) and Mg–Bi@Mg (40 686 Ω) is significantly reduced. This situation suggests that Mg–Sn@Mg and Mg–Bi@Mg can promote the charge transfer kinetics and guide the deposition of Mg at the interface between the host and the electrolyte.

In addition to improving the kinetics of Mg plating/stripping, Mg–Sn@Mg and Mg–Bi@Mg also play a crucial role in reducing the Mg nucleation overpotential (NOP: the difference between the voltage dip and the stable voltage plateau). As shown in Fig. 3f and g, the NOP of Mg–Sn@Mg at a current density of 0.1 mA cm^{-2} has a very low value of 0.218 V com-

Published on 04 travnja 2024. Downloaded on 5.6.2026. 21:53:00.

pared to that of bare Mg (0.498 V). Similarly, the NOP of Mg–Bi@Mg also has a lower value of 0.348 V at 0.1 mA cm^{-2} (Fig. 3h). The NOP values of Mg–Sn@Mg and Mg–Bi@Mg exhibit less fluctuation as the current density increases. Even at a high current density of 1.0 mA cm^{-2}, Mg–Sn@Mg and Mg–Bi@Mg showed lower NOP values (Fig. S11†). In contrast, the NOP of bare Mg rapidly increased from 0.498 V to 0.764 V with the increase of the current density, showing a great difference in NOP values among Mg–Sn@Mg, Mg–Bi@Mg and bare Mg. According to these findings, Mg–Sn@Mg and Mg–Bi@Mg provide abundant nucleation sites as cell electrodes, which ultimately ensures more uniform Mg deposition.

EIS was used to further investigate the interfacial resistance of the symmetric cells in different cycles. The R_{ct} values of Mg–Sn@Mg and Mg–Bi@Mg (Fig. 4a–c and Tables S2–4†) in the initial state are 16 171 Ω and 58 125 Ω, respectively, which are much lower than that of the bare Mg anode (85 067 Ω). After 20 cycles, the interfacial adsorption layer of bare Mg symmetric cell may be gradually detached or destroyed due to Mg deposition, which exhibits lower interfacial impedance during the

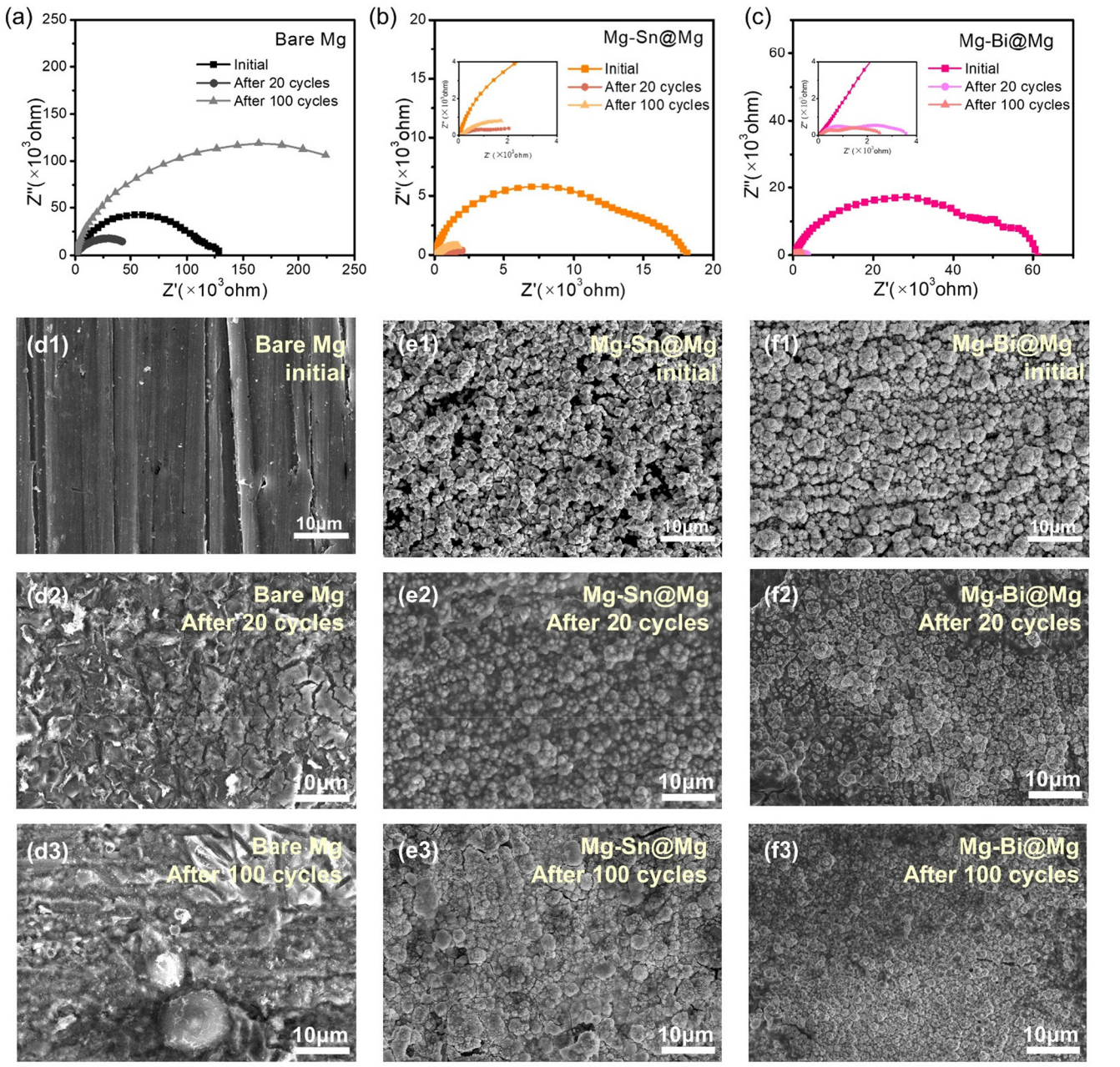

Fig. 4 (a–c) EIS for the Mg//Mg symmetric cells using (a) bare Mg, (b) Mg–Sn@Mg and (c) Mg–Bi@Mg after various cycles. SEM image of (d1–d3) bare Mg, (e1–e3) Mg–Sn@Mg and (f1–f3) Mg–Bi@Mg electrodes in symmetric cells after different cycles.

This journal is © The Royal Society of Chemistry 2024

Published on 04 travnja 2024. Downloaded on 5.6.2026. 21:53:00.

cell deposition process.[38] As shown in Fig. 4a–c, the charge transfer resistance of bare Mg decreases after 20 cycles. The R_{ct} values of both Mg–Sn@Mg (1696 Ω) and Mg–Bi@Mg (2782 Ω) are much lower than that of bare Mg cells (60 077 Ω). However, the R_{ct} of bare Mg (189 780 Ω) increases substantially after 100 cycles. The impedance of Mg–Sn@Mg (4559 Ω) and Mg–Bi@Mg (2184 Ω) still maintains a low R_{ct} even after 100 cycles, which suggests that Mg–Sn and Mg–Bi alloy layers can stabilize the interface of the anode/electrolyte. Furthermore, the evolution of the morphology of plated magnesium electrodes with an areal capacity of 0.1 mA h cm^{-2} was examined with various cycles using SEM (Fig. 4d1–d3, e1–e3, and f1–f3), and the transformation process of the produced protective layers of Mg–Sn@Mg and Mg–Bi@Mg was visible. Pits started to form on the magnesium metal anode after the 20 plating/stripping cycles, and they tended to get bigger and enlarge throughout the following cycles (Fig. 4d3). These pits may disrupt the integrity of the Mg anode, leading to the formation of an inhomogeneous Mg coating during subsequent cycling.[38] Interestingly, compared to bare Mg, the surfaces of Mg–Sn@Mg and Mg–Bi@Mg are relatively smooth and still mainly retain their initial structures (Fig. 4e2, e3 and f2, f3). After 20 and 100 cycles, the structure of the Mg–Sn@Mg and Mg–Bi@Mg anodes remained relatively compact and consistent. Even after 200 cycles, the Mg–Sn@Mg and Mg–Bi@Mg anodes presented a flat and homogeneous surface (Fig. S12 and S13†). This morphological analysis further indicates that Mg deposition is more favorable in the structures of the Mg–Sn and Mg–Bi alloy-based protective layers for Mg–Sn@Mg and Mg–Bi@Mg anodes.

Fig. S14 and S15† show the XRD patterns of Mg–Sn@Mg and Mg–Bi@Mg after magnesiation and 10 cycles. At the magnesiated state, Mg_2Sn (JCPDS no. 07-0274) can be found in the XRD pattern of the magnesiated Mg–Sn@Mg anode (Fig. S14†), and Mg_3Bi_2 (JCPDS no. 04-0464) is found in the XRD pattern of the magnesiated Mg–Bi@Mg anode (Fig. S15†). After 10 cycles, Mg_2Sn and Mg_3Bi_2 are still observed in the Mg–Sn@Mg and Mg–Bi@Mg anodes, respectively. Therefore, Mg^{2+} maybe undergoes alloying reactions with Sn and Bi during cycling, respectively. The reaction equations are as follows:

$$3Mg^{2+} + 2Bi + 6e^- \rightleftharpoons Mg_3Bi_2 \quad (2)$$

$$2Mg^{2+} + Sn + 4e^- \rightleftharpoons Mg_2Sn \quad (3)$$

To further characterize the deposition morphology on the Mg anode surface, the different behaviors of Mg-X alloy-based and bare Mg anodes during magnesium electroplating were visualized by *in situ* optical microscopy using a symmetric cell (ESI Movie 1†). Fig. 5a, b and c show the Mg deposition process for Mg–Sn@Mg, Mg–Bi@Mg and bare Mg. Obviously, metal Mg was densely and uniformly deposited on the anode surfaces of Mg–Sn@Mg and Mg–Bi@Mg without dendrite growth within 30 min at a current density of 4.0 mA cm^{-2}. It is also demonstrated that the magnesium deposition behavior is predicted to be regulated by the Mg–Sn@Mg and Mg–Bi@Mg alloy anodes. In contrast, bare Mg showed uneven Mg deposits only after 5 min of Mg plating. As plating time increases, these protrusions rapidly grow into dendrites due to uneven electric field distribution and increasing tip effect (Fig. 5c).

SEM images, XRD patterns and *in situ* optical visualization observations mentioned above demonstrate that the deposits are uniformly distributed on the surface of the Mg–Sn@Mg and Mg–Bi@Mg electrodes without large protrusions during the plating process (Fig. 5d). In contrast, bare Mg electrode produced greatly inhomogeneous deposits and the surface was severely damaged after several cycles. In addition, the presence of inhomogeneous Mg deposits leads to a porous "dead" Mg layer during cycling, which can lead to short-circuiting of the battery and other safety hazards.[59]

To further evaluate the practical applicability of Mg–Sn@Mg and Mg–Bi@Mg, we prepared and tested the full cells using Mo_6S_8 as the cathode. The full cells were measured in an APC electrolyte. First, the full cells were evaluated using cyclic voltammetry (CV). The initial CV curves (Fig. S16†) of Mo_6S_8// bare Mg, Mo_6S_8//Mg–Sn@Mg, and Mo_6S_8//Mg–Bi@Mg were tested at 0.2 mV s^{-1} in the voltage range of 0.2–1.95 V. Both Mo_6S_8//Mg–Sn@Mg and Mo_6S_8//Mg–Bi@Mg exhibit a decrease in voltage polarization (≈0.620 V and 0.473 V, respectively). This suggests that the full-cell reaction kinetics of Mg–Sn@Mg and Mg–Bi@Mg and electrochemical performance were significantly improved. We also performed CV tests at different scan rates from 0.1 to 1.0 mV s^{-1} (Fig. 6a–c) to calculate the Mg^{2+} diffusion coefficients ($D_{Mg^{2+}}$) based on the Randles–Sevcik equation:[60]

$$I_{peak} = 2.69 \times 10^5 n^{1.5} A D_{Mg^{2+}}{}^{0.5} C_{Mg^{2+}} v^{0.5} \quad (4)$$

where I_{peak} is the peak current, A is the contact surface area of the electrochemically active material, n is the number of electron equivalents per reaction species, c is the Mg^{2+} concentration in the aqueous electrolyte, and v is the scan rate. As shown in Fig. 6d, the cathode I_{peak} (C1) and anode I_{peak} (A1) show a linear relationship with the square root of v ($v^{0.5}$), implying diffusion-controlled cell kinetics. The values of the A and C peaks of the Mo_6S_8//Mg–Sn@Mg cell calculated from the linear fitting slope are 4.53×10^{-9} and 4.20×10^{-9} cm^2 s^{-1} (Table S5†), respectively. The values of the A and C peaks of the Mo_6S_8//Mg–Bi@Mg cell are 5.51×10^{-9} and 4.72×10^{-9} cm^2 s^{-1}, respectively. Both of these values exceed the values of Mo_6S_8//bare Mg (the values of peaks A and C are 3.20×10^{-9} and 2.75×10^{-9} cm^2 s^{-1}, respectively). The high $D_{Mg^{2+}}$ of the full cells of Mg–Sn@Mg and Mg–Bi@Mg accelerates the transmission speed of Mg^{2+}. Similarly, the Mg^{2+} ion transport rate of Mo_6S_8//Mg–Cu@Mg is much higher than that of bare Mg, as shown in Fig. S17.† Subsequent EIS tests on the resistance of the full cells (Fig. S18 and Table S6†) show that the R_{ct} values of the Mg–Sn@Mg and Mg–Bi@Mg full cells are much lower than that of the bare Mg cells.

As shown in Fig. 6e, Mo_6S_8//Mg–Sn@Mg and Mo_6S_8//Mg–Bi@Mg full cells show excellent rate performance at gradually increasing current density. The Mo_6S_8//Mg–Sn@Mg full cell

Published on 04 travnja 2024. Downloaded on 5.6.2026. 21:53:00.

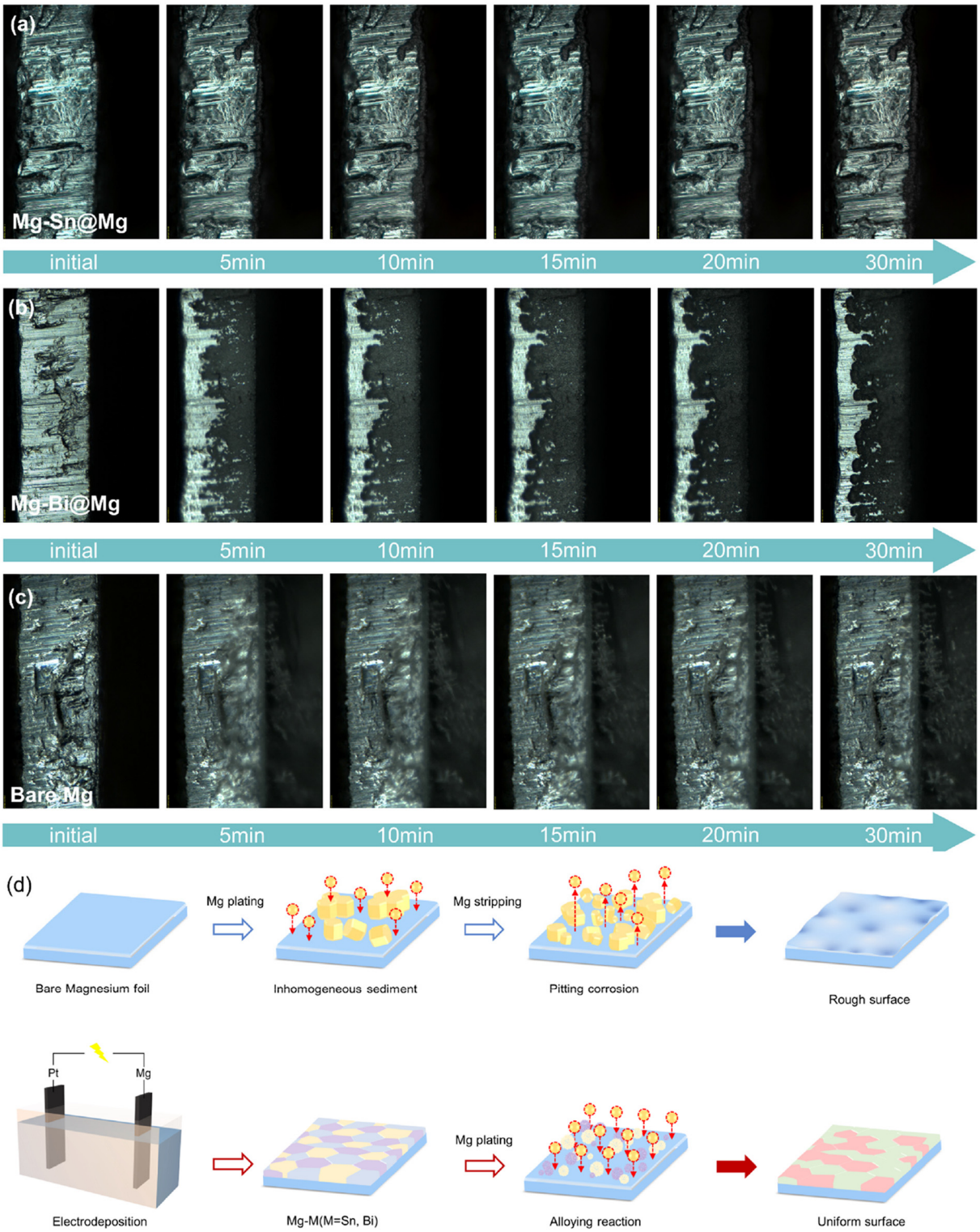

Fig. 5 (a–c) *In situ* optical visualization observations of the Mg deposition. (d) Schematics of the electrochemical behavior of bare Mg and Mg–M@Mg (M = Tin and Bismuth) anodes.

shows specific capacities of 107.4, 94.1, 81.2, 72.0, 63.9 and 52.8 mA h g^{-1} at different rates of 0.1, 0.2, 0.5, 1, 2 and 5C, respectively (Fig. S19†). The specific capacities recorded for Mo_6S_8//Mg–Bi@Mg (Fig. S20†) at the same current densities are 98.8, 90.4, 78.5, 68.4, 60.1 and 49.4 mA h g^{-1}, respectively. Both Mo_6S_8//Mg–Sn@Mg and Mo_6S_8//Mg–Bi@Mg are much better than Mo_6S_8//bare Mg (specific capacities of 96.1, 83.6, 68.4, 56.5, 47.8 and 37.6 mA h g^{-1} at different rates of 0.1, 0.2,

This journal is © The Royal Society of Chemistry 2024

Published on 04 travnja 2024. Downloaded on 5.6.2026. 21:53:00.

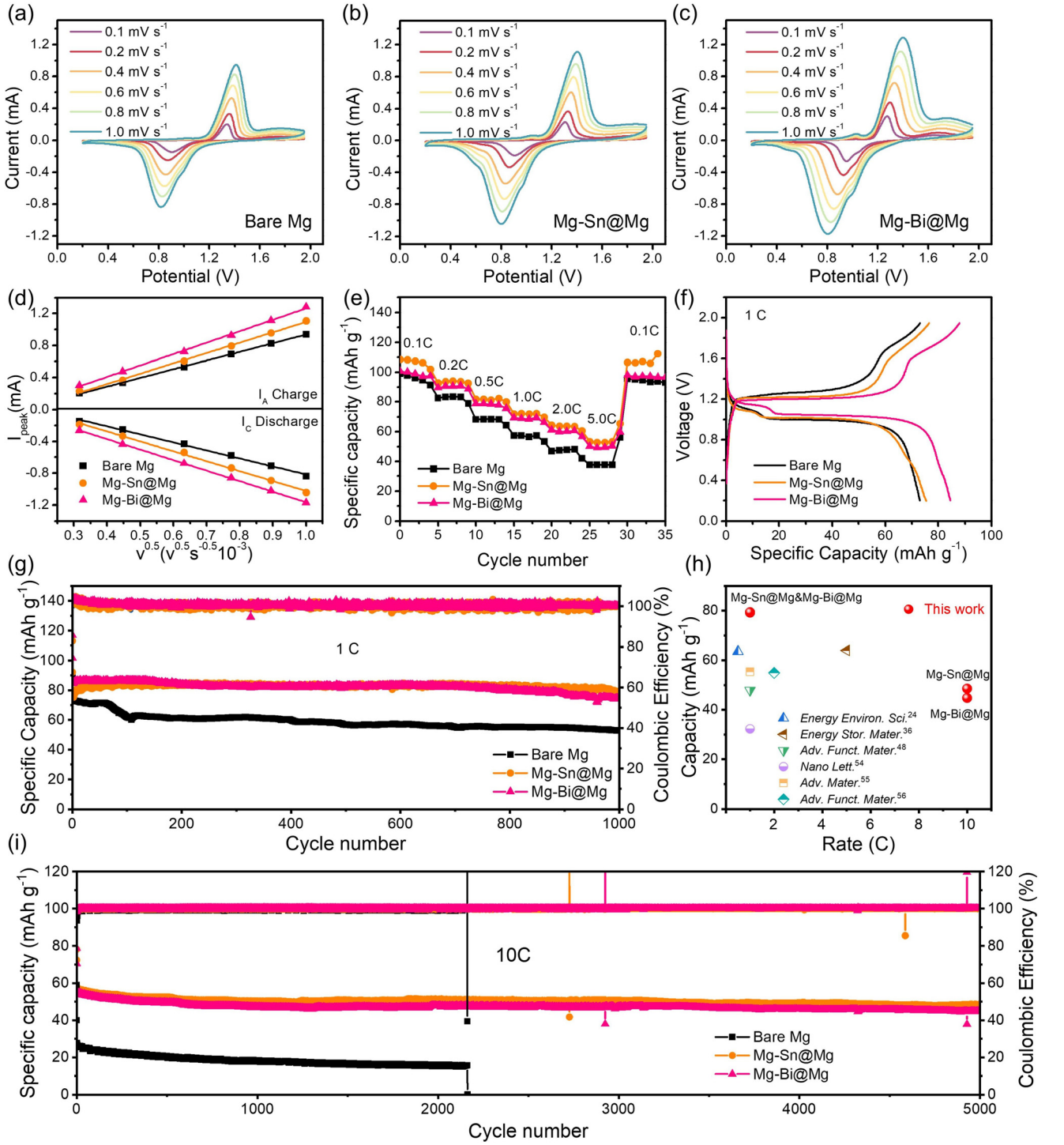

Fig. 6 CV curves of (a) Mo_6S_8//bare Mg, (b) Mo_6S_8//Mg–Sn@Mg and (c) Mo_6S_8//Mg–Bi@Mg full cells at different scan rates from 0.1 to 1.0 mV s^{-1} in the voltage range of 0.2–1.95 V and (d) the square root of scan rate ($v^{0.5}$) of bare Mg, Mg–Sn@Mg and Mg–Bi@Mg full cells. (e) Rate performance of the Mo_6S_8//bare Mg, Mo_6S_8//Mg–Sn@Mg and Mo_6S_8//Mg–Bi@Mg full cells. (f) The first charge–discharge profiles for Mo_6S_8//bare Mg, Mo_6S_8//Mg–Sn@Mg and Mo_6S_8//Mg–Bi@Mg full cells at 1 C. (g) Cycling performance of the Mo_6S_8//bare Mg, Mo_6S_8//Mg–Sn@Mg and Mo_6S_8//Mg–Bi@Mg full cells at 1 C. (h) The capacity and cycling stability performance of the Mo_6S_8//Mg–Sn@Mg and Mo_6S_8//Mg–Bi@Mg cells compared with those of previously reported Mo_6S_8//Mg full cells.[26,38,55,61–63] (i) Cycling performance of Mo_6S_8//bare Mg, Mo_6S_8//Mg–Sn@Mg and Mo_6S_8//Mg–Bi@Mg full cells at 10 C.

Published on 04 travnja 2024. Downloaded on 5.6.2026. 21:53:00.

0.5, 1, 2 and 5C, respectively) (Fig. S21†). The excellent multiplicative performance of Mo_6S_8//Mg–Sn@Mg and Mo_6S_8//Mg–Bi@Mg full cells is attributed to the Mg deposition kinetics associated with the enhanced diffusion rate of Mg^{2+} ions.

In addition to the excellent rate performance, the Mo_6S_8//Mg–Sn@Mg and Mo_6S_8//Mg–Bi@Mg cells also possess extraordinary cycling stability. The first charge–discharge profiles at 1 C are shown in Fig. 6f, and the capacities of both Mg–Sn@Mg and Mg–Bi@Mg are higher than that of bare Mg. At a current density of 1 C (Fig. 6g), Mo_6S_8//Mg–Sn@Mg and Mo_6S_8//Mg–Bi@Mg cells can deliver high discharge capacities of 79.2 and 74.6 mA h g^{-1} after 1000 cycles, respectively. Mo_6S_8//Mg–Sn@Mg and Mo_6S_8//Mg–Bi@Mg full cells have significant capacity retention rates of 85.9% and 87.0%, corresponding to the average Coulomb efficiency of 99.79% and 99.86%, respectively. Moreover, the Mo_6S_8//Mg–Cu@Mg cell also exhibits excellent cycling stability, with a high specific capacity of 81.8 mA h g^{-1} after 700 cycles (Fig. S22†). As shown in Fig. S23,† the Mo_6S_8//Mg–Sn@Mg and Mo_6S_8//Mg–Bi@Mg full cells exhibit stable performance and good capacity retention at 0.5 C. Such cycling performance of full cells using Mg–Sn@Mg and Mg–Bi@Mg exceeds that of other full cells using Mo_6S_8 as cathodes (Fig. 6h), featuring the merits of Mg–Sn@Mg and Mg–Bi@Mg. At a high current rate of 10C (Fig. 6i), the Mo_6S_8// bare Mg cell shows rapid capacity decay over 2163 cycles. Notably, the initial discharge capacity of the Mo_6S_8// bare Mg cell is 40.0 mA h g^{-1}. However, the Mo_6S_8// Mg–Sn@Mg and Mo_6S_8//Mg-Bi@Mg batteries maintained high specific capacities of 48.6 and 44.8 mA h g^{-1} after 5000 cycles.

Conclusion

In summary, Mg–Sn and Mg–Bi alloy layers were successfully constructed on magnesium metal by a facile alloy electrodeposition strategy, which significantly solved the problems of slow Mg^{2+} ion transfer kinetics and unstable anode/electrolyte interfaces, and thus improved the cycling performance of magnesium metal anodes. The as-prepared Mg–Sn@Mg and Mg–Bi@Mg symmetric cells exhibit ultra-stable cycling performance (~1000 h) at low current densities (0.1 mA cm^{-2} and 0.2 mA cm^{-2}) and a higher current density (1.0 mA cm^{-2}). More importantly, compared with the Mo_6S_8//Mg full cell, the Mo_6S_8//Mg–Sn@Mg and Mo_6S_8//Mg–Bi@Mg full cells maintained an ultra-stable electrochemical performance even after 5000 cycles. This work provides a simple and low-cost strategy to optimize the Mg metal anode interface, which would be a promising direction for the design of high-performance RMBs and it may shed light on the development of next-generation rechargeable multivalent metal batteries.

Author contributions

H. T. conceived the idea for the project and conducted the project. X. C., Y. X., F. Z., and B. H. wrote the manuscript. H. X. helped X. C. prepare alloy anodes in this work. All the authors agreed upon the final version of the manuscript.

Conflicts of interest

The authors declare no competing financial interest.

Acknowledgements

H. T. thanks the support Program of the National Energy Storage Industry-Education Platform (No. XM9981), the Beijing Laboratory of New Energy Storage Technology, North China Electric Power University and the Interdisciplinary Innovation Program of North China Electric Power University (No. XM2212315).

References

1 J. D. Huang, Y. H. Zhu, Y. Feng, Y. H. Han, Z. Y. Gu, R. X. Liu, D. Y. Yang, K. Chen, X. Y. Zhang, W. Sun, S. Xin, Y. Yu, H. J. Yu, X. Zhang, L. Yu, H. Wang, X. H. Liu, Y. Z. Fu, G. J. Li, X. L. Wu, C. L. Ma, F. Wang, L. Chen, G. M. Zhou, S. S. Wu, Z. G. Lu, X. T. Li, J. L. Liu, P. Gao, X. Liang, Z. Chang, H. L. Ye, Y. G. Li, L. Zhou, Y. You, P. F. Wang, C. Yang, J. P. Liu, M. L. Sun, M. L. Mao, H. Chen, S. Q. Zhang, G. Huang, D. S. Yu, J. T. Xu, S. L. Xiong, J. T. Zhang, Y. Wang, Y. R. Ren, C. P. Yang, Y. H. Xu, Y. A. Chen, Y. H. Xu, Z. F. Chen, X. W. Gao, S. D. D. Pu, S. H. Guo, Q. Li, X. Y. Cao, J. Ming, X. P. Pi, C. F. Liang, L. Qie, J. X. Wang, S. H. Jiao, Y. Yao, C. L. Yan, D. Zhou, B. H. Li, X. W. Peng, C. Chen, Y. B. Tang, Q. B. Zhang, Q. Liu, J. C. Ren, Y. B. He, X. G. Hao, K. Xi, L. B. Chen and J. M. Ma, Research Progress on Key Materials and Technologies for Secondary Batteries, *Acta Phys.-Chim. Sin.*, 2022, **38**(12), 2208008.

2 D. M. Kang, N. Hart, M. Y. Xiao and J. P. Lemmon, Short Circuit of Symmetrical Li/Li Cell in Li Metal Anode Research, *Acta Phys.-Chim. Sin.*, 2021, **37**(2), 2008013.

3 Y. Niu, D. Wang, Y. Ma and L. Zhi, Cascading V2O3/N-doped carbon hybrid nanosheets as high-performance cathode materials for aqueous zinc-ion batteries, *Chin. Chem. Lett.*, 2022, **33**(3), 1430–1434.

4 D. Li, Y. Yuan, J. Liu, M. Fichtner and F. Pan, A review on current anode materials for rechargeable Mg batteries, *J. Magnesium Alloys*, 2020, **8**(4), 963–979.

5 Q. Liu, X. Zhao and X. Yang, Revisiting the anodic stability of nickel-cobalt hydroxide/carbon composite electrodes for rechargeable Ni-Zn battery, *Chin. Chem. Lett.*, 2022, **33**(5), 2648–2652.

6 C. Xie, Q. Zhang, Z. Yang, H. Ji, Y. Li, H. Li, L. Fu, D. Huang, Y. Tang and H. Wang, Intrinsically zincophobic protective layer for dendrite-free zinc metal anode, *Chin. Chem. Lett.*, 2022, **33**(5), 2653–2657.

 This journal is © The Royal Society of Chemistry 2024

Published on 04 travnja 2024. Downloaded on 5.6.2026. 21:53:00.

7 A. El Kharbachi, O. Zavorotynska, M. Latroche, F. Cuevas, V. Yartys and M. Fichtner, Exploits, advances and challenges benefiting beyond Li-ion battery technologies, *J. Alloys Compd.*, 2020, **817**, 153261.
8 H. Dong, O. Tutusaus, Y. Liang, Y. Zhang, Z. Lebens-Higgins, W. Yang, R. Mohtadi and Y. Yao, High-power Mg batteries enabled by heterogeneous enolization redox chemistry and weakly coordinating electrolytes, *Nat. Energy*, 2020, **5**(12), 1043–1050.
9 G. Liu, Y. Tang, H. Li, J. He, M. Ye, Y. Zhang, Z. Wen, X. Liu and C. C. Li, Hydrated Eutectic Electrolytes Stabilizing Quasi-Underpotential Mg Plating/Stripping for High-Voltage Mg Batteries, *Angew. Chem., Int. Ed.*, 2023, **62**(16), e202217945.
10 C. Wang, H. Huang, X. Wu, M. Yousaf, M. Yan and Y. Jiang, Interfacial Reconstruction Toward Reversible Mg Anode in Conventional Electrolytes, *ACS Appl. Mater. Interfaces*, 2023, **15**(44), 51126–51134.
11 J. Song, E. Sahadeo, M. Noked and S. B. Lee, Mapping the Challenges of Magnesium Battery, *J. Phys. Chem. Lett.*, 2016, **7**(9), 1736–1749.
12 H. Dou, X. Zhao, Y. Zhang, W. Zhao, Y. Yan, Z.-F. Ma, X. Wang and X. Yang, Revisiting the degradation of solid/electrolyte interfaces of magnesium metal anodes: Decisive role of interfacial composition, *Nano Energy*, 2021, **86**, 106087.
13 Y. Shen, Y. Wang, Y. Miao, Q. Li, X. Zhao and X. Shen, Anion-Incorporated Mg-Ion Solvation Modulation Enables Fast Magnesium Storage Kinetics of Conversion-Type Cathode Materials, *Adv. Mater.*, 2023, **35**(19), 2208289.
14 R. C. Massé, E. Uchaker and G. Cao, Beyond Li-ion: electrode materials for sodium- and magnesium-ion batteries, *Sci. China Mater.*, 2015, **58**(9), 715–766.
15 J. W. Choi and D. Aurbach, Promise and reality of post-lithium-ion batteries with high energy densities, *Nat. Rev. Mater.*, 2016, **1**(4), 16013.
16 R. Attias, M. Salama, B. Hirsch, R. Pant, Y. Gofer and D. Aurbach, Anion Effects on Cathode Electrochemical Activity in Rechargeable Magnesium Batteries: A Case Study of V2O5, *ACS Energy Lett.*, 2019, **4**(1), 209–214.
17 D. Aurbach, Z. Lu, A. Schechter, Y. Gofer, H. Gizbar, R. Turgeman, Y. Cohen, M. Moshkovich and E. Levi, Prototype systems for rechargeable magnesium batteries, *Nature*, 2000, **407**(6805), 724–727.
18 N. Singh, T. S. Arthur, C. Ling, M. Matsui and F. Mizuno, A high energy-density tin anode for rechargeable magnesium-ion batteries, *Chem. Commun.*, 2013, **49**(2), 149–151.
19 T. Ichitsubo, T. Adachi, S. Yagi and T. Doi, Potential positive electrodes for high-voltage magnesium-ion batteries, *J. Mater. Chem.*, 2011, **21**(32), 11764–11772.
20 J. Niu, H. Gao, W. Ma, F. Luo, K. Yin, Z. Peng and Z. Zhang, Dual phase enhanced superior electrochemical performance of nanoporous bismuth-tin alloy anodes for magnesium-ion batteries, *Energy Storage Mater.*, 2018, **14**, 351–360.
21 J. Bae, H. Park, X. Guo, X. Zhang, J. H. Warner and G. Yu, High-performance magnesium metal batteries via switching the passivation film into a solid electrolyte interphase, *Energy Environ. Sci.*, 2021, **14**(8), 4391–4399.
22 R. Attias, M. Salama, B. Hirsch, Y. Goffer and D. Aurbach, Anode-Electrolyte Interfaces in Secondary Magnesium Batteries, *Joule*, 2019, **3**(1), 27–52.
23 F. Zhang, Y. Shen, H. Xu and X. Zhao, Bismuth Nanoparticle-Embedded Carbon Microrod for High-Rate Electrochemical Magnesium Storage, *ACS Appl. Mater. Interfaces*, 2023, **15**(19), 23353–23360.
24 J. Xiao, X. Zhang, H. Fan, Y. Zhao, Y. Su, H. Liu, X. Li, Y. Su, H. Yuan, T. Pan, Q. Lin, L. Pan and Y. Zhang, Stable Solid Electrolyte Interphase In Situ Formed on Magnesium-Metal Anode by using a Perfluorinated Alkoxide-Based All-Magnesium Salt Electrolyte, *Adv. Mater.*, 2022, **34**(30), 2203783.
25 D. Gu, Y. Yuan, J. Liu, D. Li, W. Zhang, L. Wu, F. Cao, J. Wang, G. Huang and F. Pan, The electrochemical properties of bismuth-antimony-tin alloy anodes for magnesium ion batteries, *J. Power Sources*, 2022, **548**, 232076.
26 Y. Sun, Y. Wang, L. Jiang, D. Dong, W. Wang, J. Fan and Y.-C. Lu, Non-nucleophilic electrolyte with non-fluorinated hybrid solvents for long-life magnesium metal batteries, *Energy Environ. Sci.*, 2023, **16**(1), 265–274.
27 K. Tang, A. Du, X. Du, S. Dong, C. Lu, Z. Cui, L. Li, G. Ding, F. Chen, X. Zhou and G. Cui, A Novel Regulation Strategy of Solid Electrolyte Interphase Based on Anion-Solvent Coordination for Magnesium Metal Anode, *Small*, 2020, **16**(49), 2005424.
28 N. N. Rajput, X. Qu, N. Sa, A. K. Burrell and K. A. Persson, The Coupling between Stability and Ion Pair Formation in Magnesium Electrolytes from First-Principles Quantum Mechanics and Classical Molecular Dynamics, *J. Am. Chem. Soc.*, 2015, **137**(9), 3411–3420.
29 Z. Li, X. Mu, Z. Zhao-Karger, T. Diemant, R. J. Behm, C. Kübel and M. Fichtner, Fast kinetics of multivalent intercalation chemistry enabled by solvated magnesium-ions into self-established metallic layered materials, *Nat. Commun.*, 2018, **9**(1), 5115.
30 J. Eaves-Rathert, K. Moyer, M. Zohair and C. L. Pint, Kinetic- versus Diffusion-Driven Three-Dimensional Growth in Magnesium Metal Battery Anodes, *Joule*, 2020, **4**(6), 1324–1336.
31 X. Liu, A. Du, Z. Guo, C. Wang, X. Zhou, J. Zhao, F. Sun, S. Dong and G. Cui, Uneven Stripping Behavior, an Unheeded Killer of Mg Anodes, *Adv. Mater.*, 2022, **34**(31), 2201886.
32 Y. Du, Y. Chen, S. Tan, J. Chen, X. Huang, L. Cui, J. Long, Z. Wang, X. Yao, B. Shang, G. Huang, X. Zhou, L. Li, J. Wang and F. Pan, Strong solvent coordination effect inducing gradient solid-electrolyte-interphase formation for highly efficient Mg plating/stripping, *Energy Storage Mater.*, 2023, **62**, 102939.
33 X. Xue, X. Song, A. Tao, W. Yan, X. L. Zhang, Z. Tie and Z. Jin, Boosting the cycling stability of rechargeable mag-

Published on 04 travnja 2024. Downloaded on 5.6.2026. 21:53:00.

nesium batteries by regulating the compatibility between nanostructural metal sulfide cathodes and non-nucleophilic electrolytes, *Nano Res.*, 2023, **16**(2), 2399–2408.

34 J. Long, Y. An, Z. Yang, G. Zhang, J. Zhang, S. Tan and Q. An, Efficient boron-based electrolytes constructed by anionic and interfacial co-regulation for rechargeable magnesium batteries, *Chem. Eng. J.*, 2023, **461**, 141901.

35 C. Hu, C. Wang, Y. Xia, F. Xu and T. Li, Metal organic frameworks derived NiSe2 microspheres wrapped with graphene as a high-performance cathode for rechargeable magnesium batteries, *Mater. Lett.*, 2023, **341**, 134241.

36 Z. Wei, R. Maile, L. M. Riegger, M. Rohnke, K. Müller-Buschbaum and J. Janek, Ionic Liquid-Incorporated Metal-Organic Framework with High Magnesium Ion Conductivity for Quasi-Solid-State Magnesium Batteries, *Batteries Supercaps*, 2022, **5**(12), e202200318.

37 L. Luo, X. Yang, Z. Gao, X. Li, J. Xu, Y. Zhang, R. Deng, G. Huang, J. Wang and F. Pan, Overcoming passivation in rechargeable magnesium batteries: Artificial solid-electrolyte interface for enhanced anode functionality, *Electrochim. Acta*, 2024, **478**, 143815.

38 T. Wen, B. Qu, S. Tan, G. Huang, J. Song, Z. Wang, J. Wang, A. Tang and F. Pan, Rational design of artificial interphase buffer layer with 3D porous channel for uniform deposition in magnesium metal anodes, *Energy Storage Mater.*, 2023, **55**, 816–825.

39 B. Yang, L. Xia, R. Li, G. Huang, S. Tan, Z. Wang, B. Qu, J. Wang and F. Pan, Superior plating/stripping performance through constructing an artificial interphase layer on metallic Mg anode, *J. Mater. Sci. Technol.*, 2023, **157**, 154–162.

40 X. Li, T. Gao, F. Han, Z. Ma, X. Fan, S. Hou, N. Eidson, W. Li and C. Wang, Reducing Mg Anode Overpotential via Ion Conductive Surface Layer Formation by Iodine Additive, *Adv. Energy Mater.*, 2018, **8**(7), 1701728.

41 J. Zhang, X. Guan, R. Lv, D. Wang, P. Liu and J. Luo, Rechargeable Mg metal batteries enabled by a protection layer formed in vivo, *Energy Storage Mater.*, 2020, **26**, 408–413.

42 Y. Li, X. Zhou, J. Hu, Y. Zheng, M. Huang, K. Guo and C. Li, Reversible Mg metal anode in conventional electrolyte enabled by durable heterogeneous SEI with low surface diffusion barrier, *Energy Storage Mater.*, 2022, **46**, 1–9.

43 Y. Wang, E. Sahadeo and S. B. Lee, An Electrochemically Polymerized Protective Layer for a Magnesium Metal Anode, *ACS Appl. Energy Mater.*, 2022, **5**(2), 2613–2620.

44 C. H. Shin, H. Y. Lee, C. Gyan-Barimah, J. H. Yu and J. S. Yu, Magnesium: properties and rich chemistry for new material synthesis and energy applications, *Chem. Soc. Rev.*, 2023, **52**(6), 2145–2192.

45 F. Zhang and X. Zhao, A covalent organic framework protection layer for highly active and stable Mg metal anode toward magnesium–sulfur batteries, *Mater. Lett.*, 2023, **350**, 134994.

46 J. A. Blazquez, R. R. Maca, O. Leonet, E. Azaceta, A. Mukherjee, Z. Zhao-Karger, Z. Y. Li, A. Kovalevsky, A. Fernandez-Barquin, A. R. Mainar, P. Jankowski, L. Rademacher, S. Dey, S. E. Dutton, C. P. Grey, J. Drews, J. Haecker, T. Danner, A. Latz, D. Sotta, M. R. Palacin, J. F. Martin, J. M. G. Lastra, M. Fichtner, S. Kundu, A. Kraytsberg, Y. Ein-Eli, M. Noked and D. Aurbach, A practical perspective on the potential of rechargeable Mg batteries, *Energy Environ. Sci.*, 2023, **16**(5), 1964–1981.

47 T. Mandai and H. Somekawa, Ultrathin Magnesium Metal Anode - An Essential Component for High-Energy-Density Magnesium Battery Materialization, *Batteries Supercaps*, 2022, **5**(9), e202200342.

48 C. J. Barile, D. J. Slotcavage, J. Hou, M. T. Strand, T. S. Hernandez and M. D. McGehee, Dynamic Windows with Neutral Color, High Contrast, and Excellent Durability Using Reversible Metal Electrodeposition, *Joule*, 2017, **1**(1), 133–145.

49 J. Pu, Z. Shen, C. Zhong, Q. Zhou, J. Liu, J. Zhu and H. Zhang, Electrodeposition Technologies for Li-Based Batteries: New Frontiers of Energy Storage, *Adv. Mater.*, 2020, **32**(27), 1903808.

50 X. Zhang, Y. Li, C. Van Goethem, K. Wan, W. Zhang, J. Luo, I. F. J. Vankelecom and J. Fransaer, Electrochemically Assisted Interfacial Growth of MOF Membranes, *Matter*, 2019, **1**(5), 1285–1292.

51 A. L. Yeang, Z. Li, S. Grunsfeld, G. R. McAndrews, Y. Cai, C. J. Barile and M. D. McGehee, Pulsed electrodeposition for dynamic windows based on reversible metal electrodeposition, *Cell Rep. Phys. Sci.*, 2023, **4**(11), 101660.

52 B.-H. Wang, Y.-G. Ma and Y. Cao, A Brief Introduction to Organic Electrodeposition and a Review of the Fabrication of OLEDs based on Electrodeposition Technology, *Chin. J. Polym. Sci.*, 2023, **41**(5), 621–639.

53 L. Piperno, G. Celentano and G. Sotgiu, Electrodeposition of Iron Selenide: A Review, *Coatings*, 2023, **13**(11), 1905.

54 W. Yuan, X. Nie, Y. Wang, X. Li, G. Ma, Y. Wang, S. Shen and N. Zhang, Orientational Electrodeposition of Highly (002)-Textured Zinc Metal Anodes Enabled by Iodide Ions for Stable Aqueous Zinc Batteries, *ACS Nano*, 2023, **17**(23), 23861–23871.

55 Y. Li, G. Yang, C. Zhang, W. Y. Lieu, C. Y. J. Lim, S. Sun, J. Wang, S. Jiang, Z. Xing, Z. Sofer, M.-F. Ng, W. Liu and Z. W. Seh, Grain-Boundary-Rich Triphasic Artificial Hybrid Interphase Toward Practical Magnesium Metal Anodes, *Adv. Funct. Mater.*, 2023, **33**(5), 2210639.

56 M. Liu, W. Yuan, G. Ma, K. Qiu, X. Nie, Y. Liu, S. Shen and N. Zhang, *In situ* Integration of a Hydrophobic and Fast-Zn2+-Conductive Inorganic Interphase to Stabilize Zn Metal Anodes, *Angew. Chem., Int. Ed.*, 2023, **62**(27), e202304444.

57 H. Tian, G. Feng, Q. Wang, Z. Li, W. Zhang, M. Lucero, Z. Feng, Z.-L. Wang, Y. Zhang, C. Zhen, M. Gu, X. Shan and Y. Yang, Three-dimensional Zn-based alloys for dendrite-free aqueous Zn battery in dual-cation electrolytes, *Nat. Commun.*, 2022, **13**(1), 7922.

58 J. Lopez, A. Pei, J. Y. Oh, G.-J. N. Wang, Y. Cui and Z. Bao, Effects of Polymer Coatings on Electrodeposited Lithium Metal, *J. Am. Chem. Soc.*, 2018, **140**(37), 11735–11744.

 This journal is © The Royal Society of Chemistry 2024

59 J. Eaves-Rathert, K. Moyer, M. Zohair and C. L. Pint, Kinetic-versus Diffusion-Driven Three-Dimensional Growth in Magnesium Metal Battery Anodes, *Joule*, 2020, **4**(6), 1324–1336.
60 N. Zhang, M. Jia, Y. Dong, Y. Wang, J. Xu, Y. Liu, L. Jiao and F. Cheng, Hydrated Layered Vanadium Oxide as a Highly Reversible Cathode for Rechargeable Aqueous Zinc Batteries, *Adv. Funct. Mater.*, 2019, **29**(10), 1807331.
61 Y. Li, G. Yang, S. Sun, C. Zhang, C. Y. J. Lim, A. J. Y. Wong, W. Y. Lieu, Z. Sofer, M.-F. Ng, W. Liu and Z. W. Seh, High Utilization of Composite Magnesium Metal Anodes Enabled by a Magnesiophilic Coating, *Nano Lett.*, 2022, **22**(16), 6808–6815.
62 Z. Song, Z. Zhang, A. Du, S. Dong, G. Li and G. Cui, Uniform Magnesium Electrodeposition via Synergistic Coupling of Current Homogenization, Geometric Confinement, and Chemisorption Effect, *Adv. Mater.*, 2021, **33**(26), 2100224.
63 A. Wang, L. Xue, L. Guo, C. Peng and J. Luo, Gradient Perovskite Ionic–Electronic Heterointerphases for Deep Cycling Mg Metal Anodes, *Adv. Funct. Mater.*, 2022, **32**(52), 2208735.

Published on 04 travnja 2024. Downloaded on 5.6.2026. 21:53:00.